Characterization of errors in the use of integrating-sphere systems in the calibration of scanning radiometers

Charles K. Gatebe,[1,*] James J. Butler,[2] John W. Cooper,[3] Matthew Kowalewski,[3] and Michael D. King[2]

[1]Goddard Earth Sciences and Technology Center, University of Maryland, Baltimore County, Baltimore, Maryland 21228, USA
[2]Earth Sciences Division, NASA Goddard Space Flight Center, Greenbelt, Maryland 20771, USA
[3]Science Systems and Applications, Inc., 10210 Greenbelt Road, Suite 600, Lanham, Maryland 20706, USA

*Corresponding author: charles.k.gatebe@nasa.gov

Received 2 July 2007; revised 8 September 2007; accepted 10 September 2007; posted 12 September 2007 (Doc. ID 84723); published 23 October 2007

Laboratory measurements were performed to characterize the geometrical effects in the calibration of the NASA's cloud absorption radiometer (CAR). The measurements involved three integrating sphere sources (ISSs) operated at different light levels and experimental setups to determine radiance variability. The radiance gradients across the three ISS apertures were 0.2%–2.6% for different visible, near-infrared, and shortwave infrared illumination levels but <15% in the UV. Change in radiance with distance was determined to be 2%–20%, being highest in the UV. Radiance variability due to the edge effects was found to be significant; as much as 70% due to the sphere aperture and <10% due to the CAR telescope's secondary mirror.

OCIS codes: 120.5800, 120.3150, 120.5630, 120.0280, 110.1220, 110.6770.

1. Introduction

The era of large aperture scanning radiometers in space began with the launch of the High Resolution Infrared Radiometer (HRIR) in August 1964 [1], and brought about new challenges in the calibration of solar reflectance bands. The U.S. National Bureau of Standards [now the National Institute of Standards and Technology (NIST)] at that time did not have radiance or irradiance standard sources that could fill a large instrument aperture to simulate an extended source, such as the Earth [2]. This led to the development of several methods involving the illumination of a flat or curved diffusing surface with light sources around the edge in an attempt to provide uniformity. These attempts, however, were disappointing because of poor uniformity as reported by Hovis and Knoll [2]. A better solution was found in the use of an internally illuminated integrating sphere with multiple lamps, providing one to 12 lamps illumination, to produce diffuse radiance at the exit port [3,4]. The work of Hardy and Pineo [5] and Walker *et al.* [6] has helped to improve the accuracy of large-area sphere sources.

Integrating spheres are now widely used and have been utilized with many instruments such as the scanners on the Landsat satellites [7], the Coastal Zone Color Scanner (CZCS) [8], the Advanced Very High Resolution Radiometer (AVHRR) [9], and more recently the Moderate Resolution Imaging Spectroradiometer (MODIS) [10], and multiangle imaging spectroradiometer (MISR) [11]. The spheres are also widely used in the calibration of airborne instruments such as the MODIS airborne simulator (MAS) [12], and ground instruments such as the AERONET sunphotometers [13].

There are known problems inherent in the use of integrating spheres in the calibration of instruments for remote sensing. According to Hovis and Knoll [2] the spectral irradiance from the sphere and the Sun peaks at different wavelengths (~805 and 550 nm, respectively). This causes a problem for instruments designed to look at the Earth in that calibration be-

0003-6935/07/317640-12$15.00/0

tween those two wavelengths is done with a different spectral radiance shapes from the sphere and the Sun. In addition, the technique used to transfer calibration makes a number of assumptions. These include the assumption that the characteristics of an integrating sphere destroy information about the geometry of the illuminating source. In the typical calibration geometry, the standard lamp is nearly a point source, whereas the large sphere is a 180° diffuse source. This assumption is responsible for the largest error in the transfer of calibration from the irradiance source to the sphere [2]. Last, the assumption that the spectral radiance of the sphere source is uniform over the emitting aperture can introduce significant errors.

In this study, we performed three primary, laboratory tests at NASA Goddard Space Flight Center's (GSFC's) Radiometric Calibration Facility (RCF) (described in Subsection 2.A) to characterize NASA's Cloud Absorption Radiometer (CAR) so as to improve its calibration accuracy. The first test involved three integrating sphere sources (ISSs) at different light levels as determined by the number of operating lamps—from 0–16 lamps. This test helped to ascertain linearity over the instrument performance range and to convert instrument digital counts into radiance units. The three ISSs used in these tests are described in Subsection 2.B under experimental setup. The second test involved measuring the responsivity of the CAR (defined here as detector output per unit of incident power at a particular wavelength) at more than nine different distances from the ISS aperture. This test helped to ascertain the sensitivity of calibration to distance of separation between the CAR and the ISSs. The third test involved determining the CAR's responsivity across its angular scan range. Results from these tests and analyses, including the geometrical simulation of the CAR responsivity are described in Section 3. Section 4 provides a summary and conclusions.

2. Calibration Setup

This section describes the laboratory facilities used, the experimental setup, and provides a brief overview of the CAR.

A. Description of the Laboratory Facilities

Radiometric calibration measurements were made at the RCF. The RCF maintains instruments and calibrated sources traceable to NIST to calibrate monitor, and assess the performance of satellite-, aircraft-, and ground-based remote sensing instrumentation. The instrumentation and sources cover wavelengths from the ultraviolet to the shortwave-infrared (0.23–2.40 μm). The RCF has a variety of laminar flow Class 10000 clean rooms that provide for calibration with a minimized risk of particulate contamination.

In advance of measurements using the CAR, all instrumentation and materials to be taken into the clean room were wiped down with alcohol, and the operators had to wear bunny suits to ensure high standards of cleanliness in the clean rooms.

Tests were performed with three ISS that are located in the RCF clean rooms. The ISSs have diameters of 1.83, 1.22, and 0.51 m and are nicknamed the Hardy sphere the Slick sphere, and the Uncle sphere, respectively. The Hardy and Slick spheres each have a circular aperture diameter of 0.25 m, whereas the Uncle sphere has a circular aperture diameter of 0.20 m. The ISSs are designed to have apertures that are large enough to overfill the field of view (FOV) of instruments calibrated in the lab, including the CAR. The lamps in the ISSs are positioned outside the FOV and are baffled (Hardy sphere only) so that radiance exiting the aperture is uniformly integrated through multiple diffuse reflections, providing a uniform field of radiance to the instrument. The Hardy and Slick spheres are configured for calibration in the visible and near-infrared (0.40–2.40 μm), whereas the Uncle sphere is configured for calibration in the ultraviolet (UV; 0.23–2.40 μm; see summary in Table 1, last row). The Hardy and Slick spheres exhibit decreasing radiance output into the UV region, resulting in a much less uniform radiation output that could affect the accuracy of calibration in the UV as shown in Subsection 3.A.

Both the Hardy and Slick spheres are internally illuminated by a maximum of 16 quartz tungsten halogen lamps, with each lamp rated at 200 and 45 W, respectively. The Uncle sphere is illuminated by a maximum of four lamps with each lamp rated at 150 W. The interiors of the Hardy and Uncle spheres are coated with a highly diffuse and reflective $BaSO_4$ paint with a typical reflectance >97% between 450 and 900 nm. The interior of the Slick sphere is comprised of Spectralon coated panels in a "Buckyball" configuration. The Hardy sphere is baffled internally to block direct and first-bounce light to improve the uniformity of the radiance at the aperture. Calibration of the Hardy and Slick spheres is traceable to NIST [14] using a Czerny Turner monochromator to transfer an irradiance calibration from a NIST 1000 W FEL type working standard irradiance lamp to each sphere. The areas of the monochromator entrance port and sphere aperture and the distance between them are then used to calculate the sphere radiance. The Uncle calibration transfer is performed in a similar fashion using an Ebert–Fastie double monochromator and several NIST 1000 W standard irradiance FEL lamps [15].

B. Instrument Description and Experimental Setup

A complete description of the CAR instrument is given by King *et al*. [16], and updated by Gatebe *et al*. [17] following an upgrade of the instrument in 2000. This brief overview, however, highlights some aspects of the instrument as illustrated in Fig. 1 and presented in Table 1.

The CAR has an instantaneous FOV (IFOV) of 1° and a 190° scan range, which defines the total field of view of the instrument. The scan mirror, canted 45° to the central axis of the telescope with a diameter of

Table 1. Current Cloud Absorption Radiometer and ISS Specifications

Angular scan range	190°
Instantaneous field of view	17.5 mrad (1°)
Pixels per scan line	382
Scan rate	1.67 scan lines per second (100 rpm)
Spectral channels (μm; bandwidth (FWHM))	14[a] (Eight continuously sampled and last six in filter wheel): 0.340 (0.009), 0.381 (0.006), 0.472 (0.021), 0.682 (0.022), 0.870 (0.022), 1.036 (0.022), 1.219 (0.022), 1.273 (0.023), 1.556 (0.032), 1.656 (0.045), 1.737 (0.040), 2.103 (0.044), 2.205 (0.042), 2.302 (0.043)
Output channels	9 channels at 16 bits
Data rate	61.85 MBits h^{-1}
Instrument mass	42 kg
Radiometric calibration	Spectral integrating sources: Hardy: diameter 1.83 m (0.25 m)[b] range 0.4–2.3 μm; inside coating - $BaSO_4$; Number of lamps: 16; 200 W/lamp; 6.51 A; lamps/PSU[c] 2; PSU model: HP 6554A; stability <0.05%. Slick: diameter 1.22 m (0.25 m)[b] range 0.4–2.3 μm; inside - Spectralon® panels; Number of lamps: 16; 45 W/lamp; 6.60 A; lamps/PSU[c]: 4; PSU model: LPS-200-H (Labsphere); stability <0.03%. Uncle: diameter 0.51 m (0.20 m)[b] range 0.23–0.40 μm; inside coating $BaSO_4$; Number of lamps: 4; 150 W/lamp; 6.00 A; lamps/PSU[c]: 4; PSU model: ATE-100-100M (Kepco); stability <0.03%.

[a]Spectral channels are named in the paper as channel 1, channel 2, . . . channel 14 following wavelength order as specified in this table.
[b]Diameter of sphere exit aperture.
[c]PSU - Power Supply Unit.

0.127 m, sweeps around the circumference of the telescope entrance collecting light through the 190° aperture at a rate of 100 scans per minute. When light rays enter the instrument aperture, rays striking the scan mirror at an angle of 45° get reflected to the telescope's primary mirror, and then are reflected to a smaller secondary spherical mirror with a diameter of 0.056 m (Fig. 1). These rays are then reflected through a hole in the center of the primary mirror and a defining field stop with a diameter of 0.005 m.

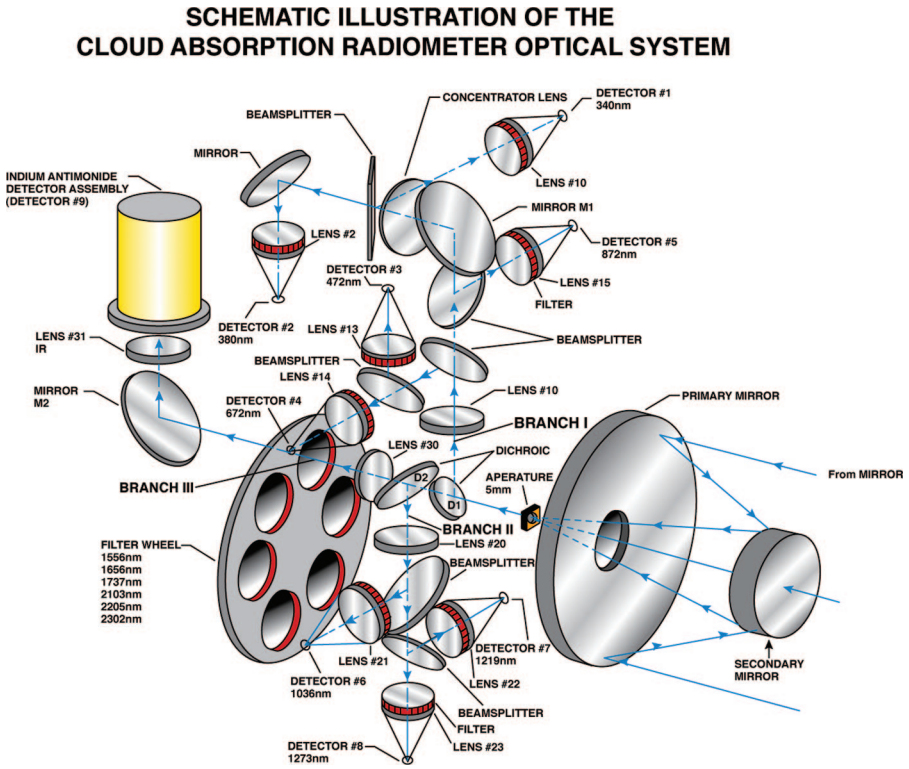

Fig. 1. Schematic of the CAR Optical System. The CAR has 14 narrow spectral bands between 0.34 and 2.30 μm, six of which (1.5–2.3 μm) are defined on the filter wheel and share one detector, while the rest have separate detectors as shown on the diagram. The CAR scans through a 190° plane with an IFOV of ~1°. Full illustration of the CAR instrument can be seen in King *et al*. [4] and Gatebe *et al*. [5].

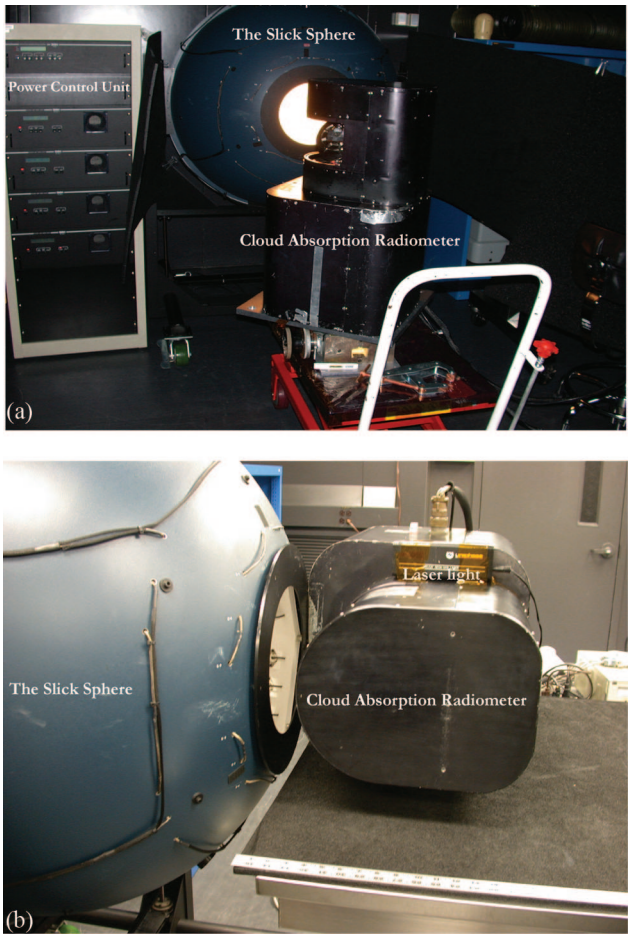

Fig. 2. Pictures showing setup for Slick sphere and CAR for determining (a) responsivity across the scan range, and (b) change in radiance with distance of separation, with the CAR at the closest distance from the Slick sphere.

The rays continue through a series of dichroic beam splitters, mirrors, narrow band interference filters, and lenses that help define light spectrally before arriving at nine different detectors [18].

The tests were performed with the CAR placed a known distance from the ISS apertures and carefully aligned to ensure that the optical axis of the instrument was perpendicular to the plane of the sphere aperture (Fig. 2). For the distance tests, the instrument-sphere separation was varied from 0.23 m (where the instrument was very close to the sphere aperture) to 4.90 m. The number of scans acquired at each distance and light level (1–16) ranged between 300 and 1000. It also should be noted that the distance tests were done only with the Slick sphere at eight-lamp and four-lamp illumination levels, and the Uncle sphere at four-lamp and two-lamp illumination levels. The Hardy sphere is located in a room that is relatively small for distance test measurements, but the sphere is too large and complex to be moved to any other room. Each ISS was stabilized for more than 1 h before measurements, and the room was kept dark during measurements to minimize any contribution from external light.

3. Results and Discussions

This section discusses results from various tests including the geometrical simulation of CAR measurements with an emphasis on calibration errors due to geometrical effects.

A. Uniformity of Radiance Across ISS Aperture

Figure 3 shows typical spectral radiance counts while viewing the Hardy sphere (in units of instrument digital counts) as measured by the CAR at half-degree intervals across the 190° scan range at different wavelengths as defined in Table 1. From this figure, the Hardy sphere was internally illuminated by six lamps, instrument-sphere distance was ~0.35 m, and the output was averaged over 360 scans. Note that the Hardy sphere was scanned vertically across the diameter of the sphere aperture. The general shape of each spectral curve looks like a flat-topped pyramid with a baseline that extends across the entire angular scan range defined by a scale in the interval: −8.25–182.5°. A gradual rise in the signal is seen in all spectral channels as the Hardy sphere aperture enters the IFOV of the CAR, reaching a peak as the aperture fills the IFOV (each CAR channel showing its own signal strength), and then drops as the aperture moves out of the IFOV. The width of the flat top depends on the distance of separation between the instrument and the sphere, being wider for short distances and narrower for long distances as the angular size of the sphere aperture decreases.

A closer look at the peak radiance from the three ISS reveals spatial gradients across the aperture, which may indicate nonuniformities in the interior surface of the ISS. To further investigate the nature of this change, all the peak values (characterized by a small coefficient of variation, <0.001) were selected

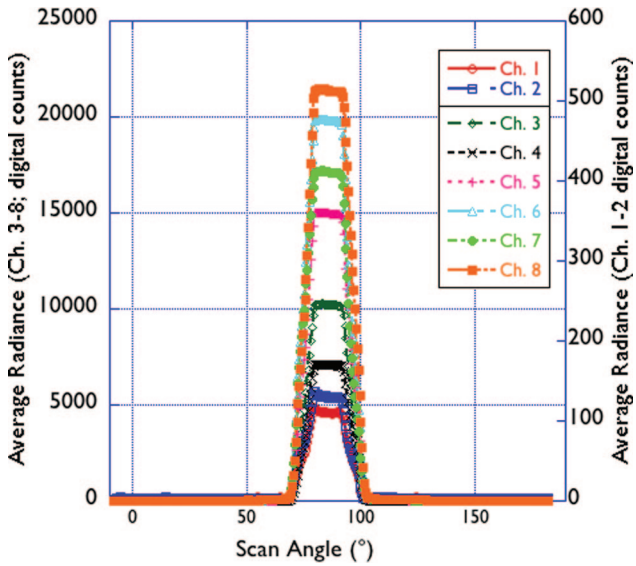

Fig. 3. (Color online) Spectral radiance output from the Hardy sphere at six-lamp level as measured by the CAR at 0.5° intervals across the 190° scan range, averaged over 360 scans. The signal is relatively flat at the peak as Hardy sphere fills the IFOV.

and analyzed separately. Figure 4(a) shows the resulting spectral radiance from the three ISS at full power as measured in channel 4 (0.682 μm), normalized to maximum peak radiance from each ISS. The Hardy sphere curve looks like a slanted sine curve, one side taller than the other, whereas the Slick and Uncle sphere curves depict a shallow dome shape. The Hardy sphere shape is caused by differences in reflectance characteristics of the two hemispheres that make up the sphere. Tables 2 and 3 show spatial gradients in radiance across each aperture at eight light levels with the instrument-sphere distance ranging from 30–50 cm. Each value is a difference between maximum and minimum radiance expressed in a percentage of average radiance across the ISS aperture, and includes an estimate of a standard error. From Table 2, the radiance gradients in the UV are relatively large (channels 1 and 2: 2–15%), but relatively low (≈1%) in the visible and near-infrared (channels 3–8). Note that some channels saturate at higher light levels. From Table 3, under the Uncle sphere at the four-lamp level, the radiance gradients are even lower in channels 1–4 (<0.5%) and <2% at the two-lamp level. It can also be seen that the Uncle sphere is too bright for most CAR channels, which leads to radiance saturation. Note that the gradients are higher in the UV (1–8%) for instrument-sphere distances >1 m, but remain small in the visible and near-infrared (<0.5%). The Slick sphere has high gradients in channel 1 (2–9%) and channel 2 (3–12%) and from 0.8–2.6% in the other channels. Ideally, the spectral radiance gradient should be <2% across a good ISS aperture [6]. The nonuniformity of the radiance output from the Slick sphere is partly due to unbaffled lamps and nonisotropic reflectance from the interior of the sphere that is made of flat Spectralon panels, which contributes to a changing bidirectional reflectance. These results demonstrate that the Hardy and Slick spheres are not configured for calibration in the UV, but are suitable for calibration in the visible and near-infrared. The Uncle sphere is suitable for calibration in the UV, visible, and near-infrared, but have higher spatial gradients (<8%) in the UV for separation distances >1 m.

An additional mapping of radiance uniformity was done with a fiber coupler system comprising of two Ocean Optics minispectrometers (one spectrometer is configured for the UV range of 300–380 nm and the other for the visible range of 380–680 nm) for intercomparison with the CAR measurements. The spectral resolution of each spectrometer is nominally 1 nm, with sampling every 0.06 nm in the UV and 0.5 nm in the visible. Measurements were made at 22 × 22 cm grid points across the face of the aperture of the Uncle sphere for an instrument-sphere distance of 25 cm. In order to improve the signal-to-noise ratio, data were binned into 5 nm spectral bins. Figures 4(b) and 4(c) show the results from the Uncle sphere at four-lamp levels at two wavelengths corresponding to CAR channels 1 and 2, normalized to the radiance output from a point in the center of the grid.

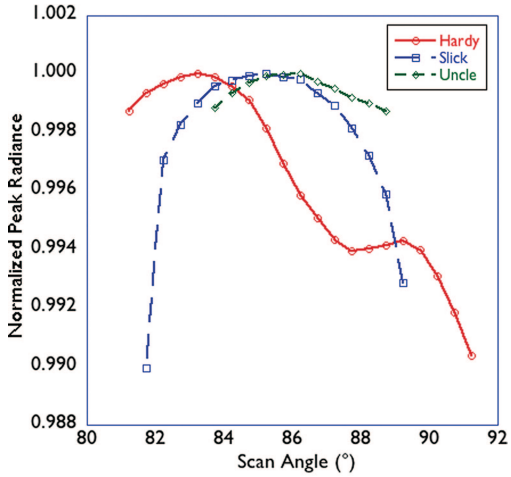

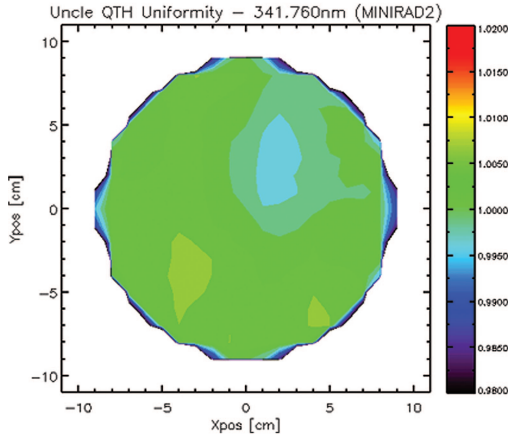

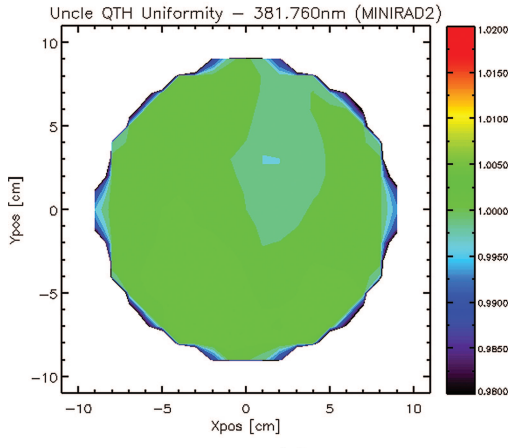

Fig. 4. (a) Radiance measured in channel 4 (0.682 μm) across the three ISS apertures and normalized to their maximum peak radiance. The three ISSs were operated at full power with the Hardy sphere and Slick sphere internally illuminated by 16 lamps and the Uncle sphere by four lamps. (b) Relative response at 342 nm normal to the Uncle sphere exit aperture plane viewed with Ocean Optics mini-spectrometers with a 2° FOV. The sphere was illuminated at full power (four-lamp level). (c) Relative response at 382 nm normal to the Uncle sphere exit aperture plane viewed with Ocean Optics mini-spectrometers with a 2° FOV. The sphere was illuminated at full power (four-lamp level).

Table 2. Spatial Gradient of Radiance at Points-Across the Hardy Sphere Aperture (in percent)[a]

Channel	One Lamp	Two Lamps	Three Lamps	Four Lamps	Five Lamps	Six Lamps	12 Lamps	16 Lamps
1	10.71 ± 0.97	4.30 ± 0.51	3.38 ± 0.34	4.36 ± 0.30	4.21 ± 0.26	4.06 ± 0.21	3.09 ± 0.08	4.87 ± 0.05
2	14.59 ± 0.86	4.81 ± 0.45	4.34 ± 0.30	4.11 ± 0.26	3.37 ± 0.23	3.31 ± 0.18	2.81 ± 0.07	3.78 ± 0.04
3	1.57 ± 0.01	1.17 ± 0.00	1.24 ± 0.00	1.24 ± 0.00	1.29 ± 0.00	1.22 ± 0.00	1.25 ± 0.00	1.24 ± 0.00
4	1.21 ± 0.00	0.90 ± 0.00	0.97 ± 0.00	0.98 ± 0.00	1.01 ± 0.00	0.95 ± 0.00	0.97 ± 0.00	0.97 ± 0.00
5	1.21 ± 0.00	0.90 ± 0.00	0.96 ± 0.00	0.96 ± 0.00	1.01 ± 0.00	0.95 ± 0.00	Saturated	Saturated
6	1.18 ± 0.00	0.87 ± 0.00	0.93 ± 0.00	0.93 ± 0.00	0.98 ± 0.00	0.91 ± 0.00	Saturated	Saturated
7	1.05 ± 0.00	0.85 ± 0.00	0.91 ± 0.00	0.93 ± 0.00	0.98 ± 0.00	0.92 ± 0.00	1.01 ± 0.00	Saturated
8	1.24 ± 0.00	0.72 ± 0.00	0.75 ± 0.00	0.74 ± 0.00	0.78 ± 0.00	0.73 ± 0.00	Saturated	Saturated

[a]The values are calculated from the difference between maximum and minimum radiance, normalized to the average radiance over all points across the Hardy sphere aperture at a given light level. The error is defined by the standard error (standard deviation/square root of N; where N is the number of scans).

The largest deviation was ≈2%, seen around the edge of the sphere. These results are in general agreement with those obtained with the CAR.

B. Responsivity Across the Angular Scan Range

Since the CAR scan range is wide, and the sphere aperture takes up a relatively small angular portion (Figs. 2 and 3), measurements were made with the Slick sphere illuminated by four lamps and positioned at different angular distances within the 190° angular scan range. From Fig. 5, the maximum peak radiance in channels 1–8 is shown for various angular scan angles, normalized to the maximum peak radiance in the entire angular scan range in each channel. From the figure, channels 1 and 2 are the most sensitive with minimum values in the center of the scan range (<6%). The change in radiance seen in channels 1 and 2 is significant (<6%), in comparison to channels 3–8 (<1%). This could be due to optical alignment, which would be amplified more in the shorter wavelengths. These results are not totally surprising considering that the two channels were added during the CAR upgrade in 2000 [17], which assumed that the original alignment would hold. This may need to be reassessed. In addition, this effect needs to be accounted for in the previous calibration measurements, particularly in the UV. The contrast in shape between channels 3–7 and channel 8 is noteworthy, but of little consequence to the calibration accuracy.

C. Change in Radiance with Distance

The change in radiance with distance is interesting as shown in Figs. 6(a), 6(b), and 7, and Table 4. Measurements were taken with the Slick sphere at various instrument-sphere distances ranging from 23–490 cm, and 30–421 cm with the Uncle sphere. At each distance the sphere aperture was centered within a scan angle of ≈85°. Figures 6(a) and 6(b) show only the peak radiance output in the scan range 60°–110° in a selected number of channels. The radiance pattern seen in Fig. 6(a) (channel 1; the Slick sphere) is similar to channel 2 for both the Slick and Uncle spheres. Figure 6(b) (channel 3; the Slick sphere) represents the pattern seen in channels 3–14 for both spheres. Note that in Fig. 6(a), the peak radiance initially decreases with distance and then increases beyond 46 cm as the angular size of the sphere decreases. However, the radiance for most scan angles seems to decrease with distance. The peak radiance is observed to decrease with distance in channel 3 as shown in Fig. 6(b). The change in radiance with distance seems to violate the principle that radiance is invariable in a lossless media [19], and warrants further investigation.

Table 3. Spatial Gradient of Radiance at Points Across Apertures of the Uncle Sphere and Slick Sphere (in percent)

	Uncle Sphere[a]		Slick Sphere[a]			
Channel	Two Lamps	Four Lamps	Four Lamps	Eight Lamps	12 Lamps	16 Lamps
1	1.33 ± 0.22	0.16 ± 0.28	2.72 ± 0.19	8.51 ± 0.21	7.04 ± 0.16	7.27 ± 0.14
2	1.82 ± 0.23	0.42 ± 0.30	4.38 ± 0.25	11.93 ± 0.25	3.81 ± 0.19	3.46 ± 0.14
3	0.20 ± 0.56	Saturated	1.55 ± 0.12	1.59 ± 0.33	1.49 ± 0.31	1.42 ± 0.34
4	0.12 ± 0.42	0.12 ± 0.44	1.37 ± 0.15	1.07 ± 0.35	0.86 ± 0.31	0.79 ± 0.34
5	Saturated	Saturated	1.34 ± 0.12	1.64 ± 0.38	0.96 ± 0.41	1.00 ± 0.40
6	Saturated	Saturated	1.24 ± 0.16	2.04 ± 0.95	Saturated	Saturated
7	Saturated	Saturated	1.21 ± 0.23	2.61 ± 1.19	Saturated	Saturated
8	Saturated	Saturated	1.08 ± 0.27	Saturated	Saturated	Saturated

[a]The values are calculated from the difference between maximum and minimum radiance, normalized to the average radiance over all points across each ISS aperture at a specified light level. These gradients are for short distances from the ISS apertures. The gradients are higher especially in the UV for long distances. For example, at a distance of 274 cm from the Uncle sphere aperture, the gradients in channel 1 are: 4.81% (±0.26; 4-lamp level) and 6.72% (±0.25; 2-lamp level). Channel 2: 6.29% (±0.39; 4-lamp level) and 7.60% (±0.29; 2-lamp level).

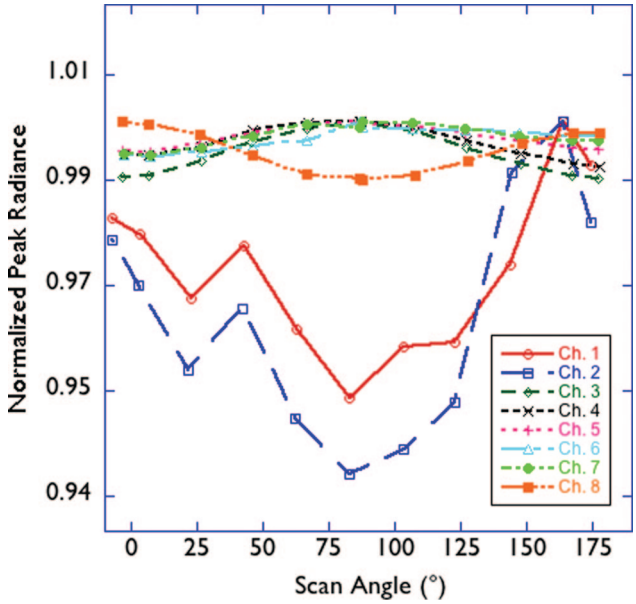

Fig. 5. (Color online) CAR responsivity within the 190° scan range with Slick sphere internally illuminated by four lamps. Each point represents maximum peak radiance at a given scan angle, normalized to the maximum peak radiance from within the 190° scan range in each channel. The UV channels (channels 1 and 2) show the highest sensitivity (4–6%), whereas channels 3–8 have lowest sensitivity (<1%).

The percentage change in radiance between d_1 = 23 cm and d_N = 490 cm is summarized in Table 4, for the Slick sphere, and between d_1 = 30 cm and d_N = 421 cm for the Uncle sphere. Note that each value is the difference between peak radiance measured closest to the aperture at d_1 = 23 cm and furthest at d_N = 490 cm as a percentage of the peak radiance at d_1 = 23 cm. The highest differences are seen in the Slick sphere (13.2% and 20.1%; channels 1 and 2, respectively) and the smallest differences are seen in the Uncle sphere (2.0% and 5.1%; channels 1 and 2, respectively). In the visible and near-infrared channels the differences range from 5.1–9.0% for both spheres. Note that the values in brackets are for lower-light levels (four-lamp level in the case of the Slick sphere and the two-lamp level in the case of the Uncle sphere), and that the CAR filter wheel was locked on channel 13 (2.2 μm) during measurements with the Uncle sphere. For the Slick sphere measurements, the filter wheel was rotated to a new wavelength after every five scans on each filter wheel channel (channels 9–14).

The radiance dependence on distance as seen from both the Slick and Uncle spheres, if found to be independent of the CAR, demands that instrument calibration measurements be done at a standard instrument-sphere distance so as to minimize errors in calibration. The calibration transfer from the NIST 1000 W lamp is done at an instrument-sphere distance of 50 cm, and a similar setup may be considered for future instrument calibration. There are, however, other considerations in determining an optimum instrument-sphere distance. For example, Fig. 7 shows the average radiance from the Slick and Uncle spheres at various instrument-sphere distances, normalized to maximum peak radiance at each distance. The average radiance in channels 1 and 2 shows a decreasing trend with distance, but increases beyond d = 132 cm for the Slick sphere.

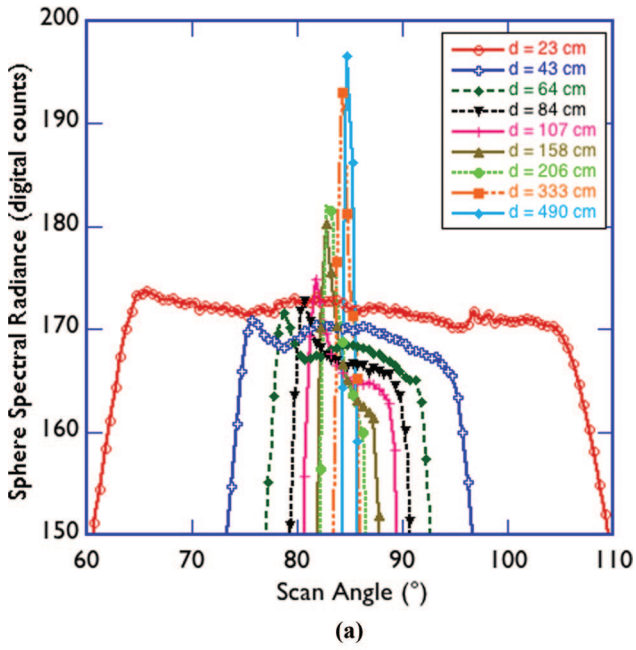

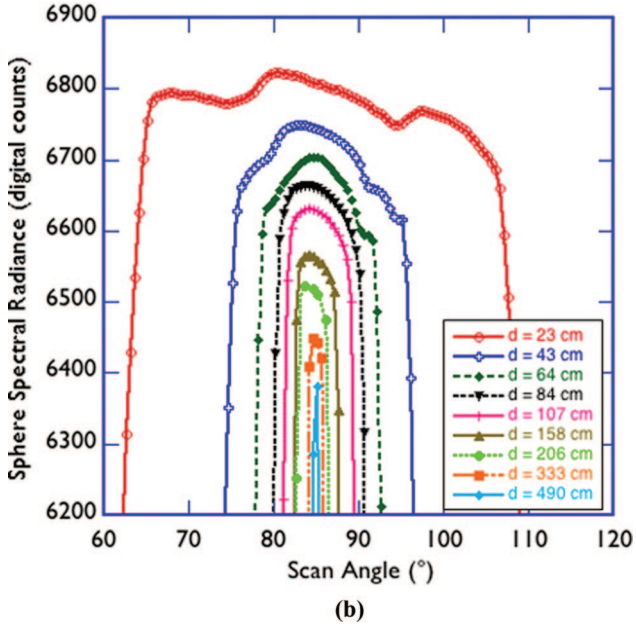

Fig. 6. (Color online) (a) Peak radiance as a function of distance in channel 1 (0.340 μm) with the Slick sphere illuminated by four lamps. The peak radiance initially decreases and then increases beyond 43 cm. The difference between maximum peak radiance at d = 23 cm and d = 490 cm is 12.3%. Similar results were seen in channel 2 (cf. Table 4). (b) Peak radiance as a function of distance in channel 3 (0.472 μm) with Slick sphere illuminated by four lamps. The peak radiance decreases with distance. The difference between maximum peak radiance at d = 23 cm and d = 490 cm is 6.7%. Similar results were seen in channels 4 to 8 (cf. Table 4).

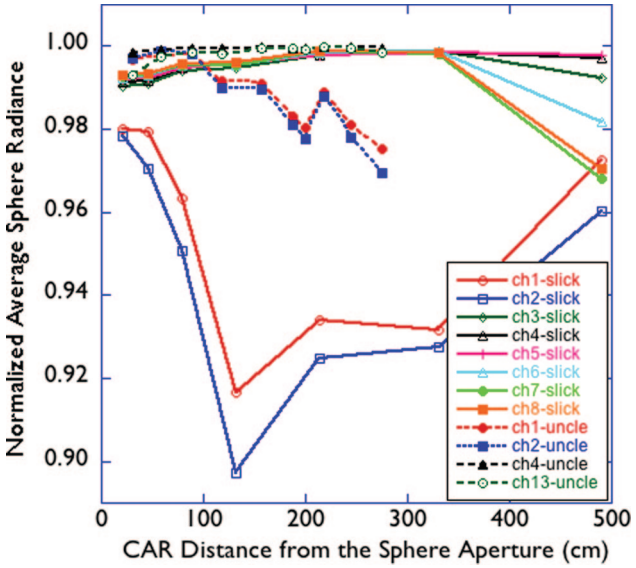

Fig. 7. (Color online) Average radiance as a function of distance with the Slick sphere internally illuminated by four lamps, normalized to peak maximum radiance in each channel at each distance. The radiance in channels 3–8 varies slightly with distance, but show spectral dispersion at the longest distance, d_N = 490 cm. Channels 1 and 2 appear different with the smallest value at d = 206 cm. (cf. Table 4).

The average radiance in channels 3–8 and 13 approaches unity. Note that measurements with the Uncle sphere were limited to a distance of up to d = 275 cm, because of its smaller aperture diameter (0.20 m). A value of 1 would imply a perfect radiance uniformity across the sphere aperture, as the average and maximum peak radiance would have the same value. The spectral radiance divergence seen at d = 490 cm is a sign of contamination from the sphere edges. From these results, and excluding channels 1 and 2, an optimum distance of separation between the instrument and sphere can be determined; the instrument should not be too close to the sphere as that would introduce nonuniformity issues, and not too far away to introduce edge effects that would be difficult to account for in calibration. However, the pattern seen in the UV defies this logic and makes calibration of the two UV channels complicated. The results from the Slick and Uncle spheres, particularly in channels 1 and 2 may suggest that the problem lies with the ISSs, especially the Slick sphere, where channels 1 and 2 are so different from the rest, and could be due to nonuniformity in the UV.

Finally, the effects of size of source and background loading (defined here as the diffuse light scattered by surfaces including the instrument casing, integrating sphere's outer surface, and the surrounding walls back into the IFOV of the CAR) may be important and are yet to be determined. These effects could conceivably enhance the signal, especially when an instrument is very close to a source and is not equipped with a good mechanism to suppress stray light. The CAR telescope, however, is equipped with a baffle that is designed to remove the stray light. The effectiveness of this baffle system was confirmed with a simple "lollipop test," where laboratory measurements were done while blocking light from the sphere with a specially darkened circularly shaped lollipop, and repeating the measurements without the lollipop, and comparing instrument responsivity with and without the lollipop. The results showed no significant stray light problem. And the signal enhancement due to the loading effect was found to be quite small as determined from measurements in directions away from the sphere aperture. However, a point spread response function would be more reliable, and hopefully will be determined in the future to put this matter to rest [20]. (Steven Brown, NIST, personal communication).

Table 4. Difference Between Maximum Peak Radiance at Distance d_1 and d_N Relative to Radiance at d_1 (Slick Sphere d_1 = 23 cm and d_N = 490 cm, and Uncle Sphere d_1 = 30 cm, d_N = 421 cm)[a]

Channel	Slick Sphere (%)	Uncle Sphere (%)
1	13.2 (12.3)	2.0 (6.1)
2	20.1 (18.7)	5.1 (8.4)
3	−6.5 (−6.4)	Saturated (−6.1)
4	−5.9 (−5.4)	−5.1 (−5.1)
5	−6.5 (−6.5)	Saturated
6	−7.2 (−7.6)	Saturated
7	−8.9 (−8.0)	Saturated
8	Saturated (−7.9)	Saturated
9	−9.0 (−7.4)	No measurements
10	−8.8 (−7.4)	No measurements
11	−8.8 (−7.3)	No measurements
12	−8.2 (−6.3)	No measurements
13	−7.7 (−6.7)	−5.9 (−6.3)
14	−7.1 (−6.8)	No measurements

[a]Values are for two light levels: Slick: eight-lamp level (four-lamp level); Uncle: four-lamp level (two-lamp level).

D. Linearity Tests

The linearity tests involved measuring the radiance of the three ISS illuminated at different lamp illumination levels ranging from 0–16, covering a wide dynamic range of the CAR detectors. The illumination levels were varied in steps of one lamp for the Hardy sphere and four lamps for the Slick sphere up to a maximum of 16 lamps. The illumination levels for the Uncle sphere were varied in steps of two lamps up to a maximum of four lamps. For all channels, a linear response with a correlation coefficient of 1 was established and applied to an equation of the form: $L = mc + b$, where L is the spectral radiance, m is the inverse of the CAR responsivity, c is the digital count, and b is the offset. Figure 8 illustrates the procedure used to derive this linear relationship. For example, typical calibration coefficients established for channel 3 (0.472 μm) are m = 0.0096 W m^{-2} sr^{-1} μm^{-1} count^{-1} and the intercept, b = 0.0981 W m^{-2} sr^{-1} μm^{-1}, while for channel 8 (1.273 μm) the calibration slope m = 0.0132 W m^{-2}sr^{-1} μm^{-1} count^{-1} and the intercept, b = 0.6284 Wm^{-2} sr^{-1} μm^{-1}.

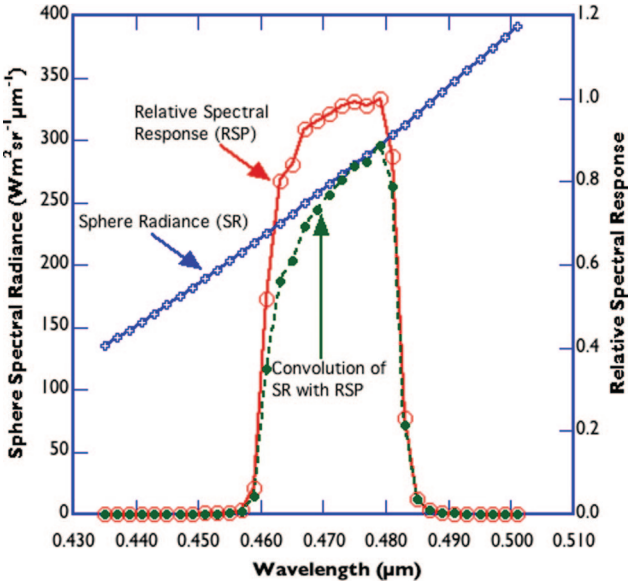

Fig. 8. (Color online) The Hardy sphere radiance (SR curve; from GSFC's radiometric calibration) and CAR relative spectral response function (RSP curve; from previous measurements as described in Gatebe *et al*. 2003) in channel 3 (central wavelength at 0.472 μm). A convolution of SR and RSP is obtained from a product of sphere radiance (SR curve) and relative spectral response (RSP curve). The integral of the product (combined SR and RSP curve) divided by the integral of the RSP curve gives the band weighted sphere radiance, which is equivalent to the CAR digital counts in channel 3. This procedure is repeated with different sphere output, usually spanning the entire detector dynamic range. A plot of the derived radiance versus corresponding digital counts gives a linear relationship whose coefficients define CAR responsivity and offset. These coefficients are used to convert instrument digital count to radiance as described in Section D.

E. Edge Effects from the Sphere and Instrument Telescope Mirror

Figure 9 shows the standard deviations derived from results shown in Fig. 3 for an average of 360 scans. The standard deviations show very distinct peaks coinciding with signal rise and fall as shown in Fig. 10. The standard deviation curves flatten outside and inside the Hardy sphere aperture when the source is either completely outside or completely within the IFOV of the CAR. It is noted that peak values have a very low coefficient of variation (<0.001) and those outside have higher values (>0.1). The height or magnitude of the standard deviation peaks depends on the separation distance between the CAR and the sphere. Figure 11 shows variations of the standard deviation peaks at selected distances from the Slick sphere in channel 3. Note that a similar pattern is seen in the other channels and other ISS. At $d = 64$ cm, the angular distance of the standard deviation peaks are further apart and have lower magnitude compared with the other distances. At $d = 490$ cm, only two peaks are observed. Note, however, that with the Uncle sphere, channels 1 and 2 depicted four peaks even at long distances. In the next section, we will use geometrical simulations to

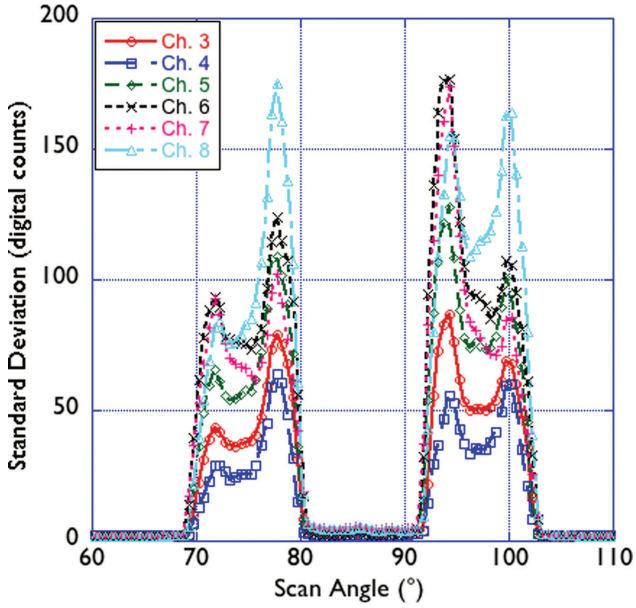

Fig. 9. (Color online) Standard deviation derived from the Hardy sphere measurements shown in Fig. 3. The standard deviation peaks correspond to when the Hardy sphere aperture enters or leaves the CAR IFOV. The noise pattern is thought to be unique to scanning radiometers as an ISS aperture moves in or out of the IFOV.

shed light onto these measurements and show the cause of the observed standard deviation peaks.

F. Simulation Results

We have simulated the radiance seen by the CAR with two nonconcentric circles, representing the CAR IFOV of radius r and an ISS aperture of radius R .The area of intersection is obtained using the formula for the circular segment in the form:

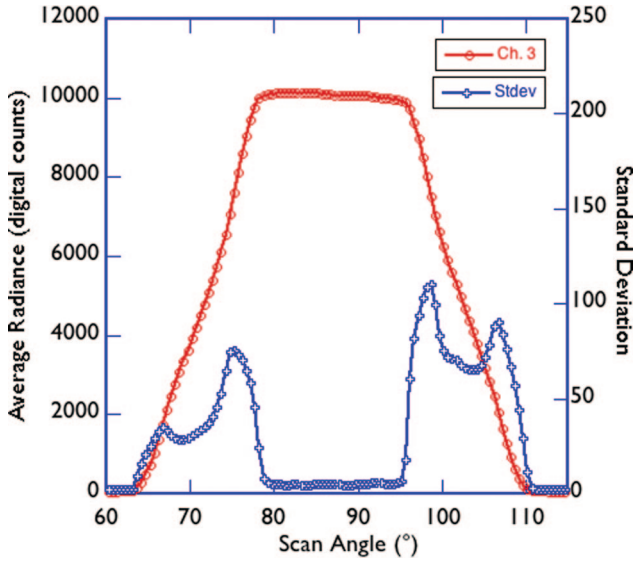

Fig. 10. (Color online) Mean spectral radiance in channel 3 and its standard deviation. Notice the peaks coincide with the sloping areas of the radiance curve.

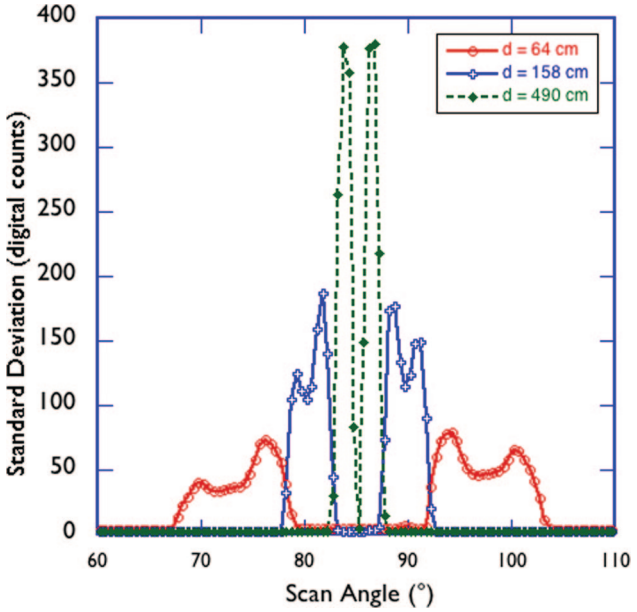

Fig. 11. (Color online) Standard deviation curves from measurements made at selected distances between the CAR and Slick sphere to show the noise pattern dependence on distance. As the Slick sphere becomes more distant, the standard deviation peaks reduces from four to two, whereas the magnitude increases.

$$A = r^2 \cos^{-1}\left(\frac{d^2 + r^2 - R^2}{2dr}\right) + R^2 \cos^{-1}\left(\frac{d^2 + R^2 - r^2}{2dR}\right) - \frac{1}{2}\sqrt{(-d + r + R)(d + r - R)(d - r + R)(d + r + R)}, \quad (1)$$

where A is the area of intersection, r the radius of the CAR's IFOV, R the radius of the ISS aperture, and d the distance between the centers of the CAR IFOV and the ISS aperture. For a derivation of Eq. (1), see Weisstein [21].

A plot of the area of intersection as a function of distance between the center of the CAR IFOV and ISS aperture shows a pattern that is similar to the actual measurements, but the rise or fall appears more uniform than observed (Figs. 10 and 12). When random noise (representing small jitter in the scan mirror of 0.01) is added to the distance between the centers, the standard deviation peak occurs at distances defining partial overlap of the two circular areas. Further, introducing a circular hole in the center of the CAR IFOV and then recalculating the area of overlap and standard deviation gives results that are very similar to the actual measurements (Figs. 10, 12 and 13). The simulated signal shows a nonuniform rise or fall as observed in the measurements, and the random noise shows two outer peaks at the distances where the circles partially overlap. It is conceivable, therefore, that the standard deviation peaks seen in the measurement are caused by a combination of the variation in scan mirror speed and obscuration by the telescope's secondary mirror. The edge of the sphere aperture causes the first and

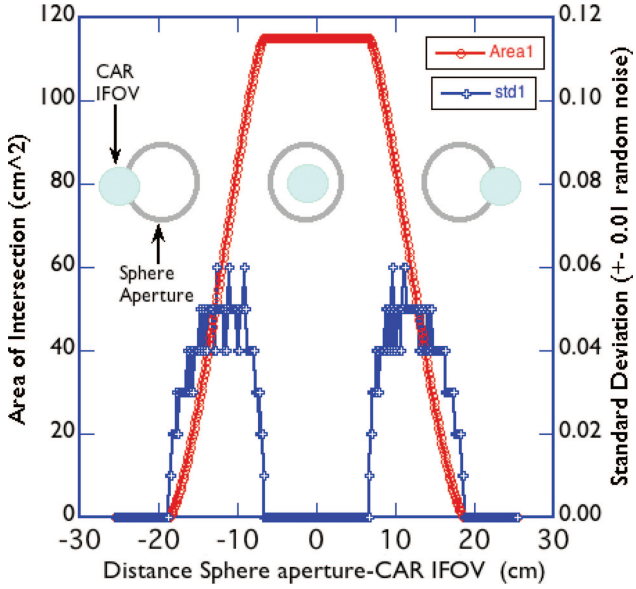

Fig. 12. (Color online) Radiance simulation from a convolution of CAR IFOV (shaded circle) and sphere aperture (open circle). The area of the sphere aperture that is inside the IFOV (area of overlap) plotted as a function of the distances between the centers of both circles, representing the signal strength. Random variations in the distance between the centers of the circles seem to introduce higher standard deviation (solid curve with + symbol) over the area of partial overlap of the two circles; an effect that is observed in our measurements. (N.B.: size of apertures not drawn to scale.)

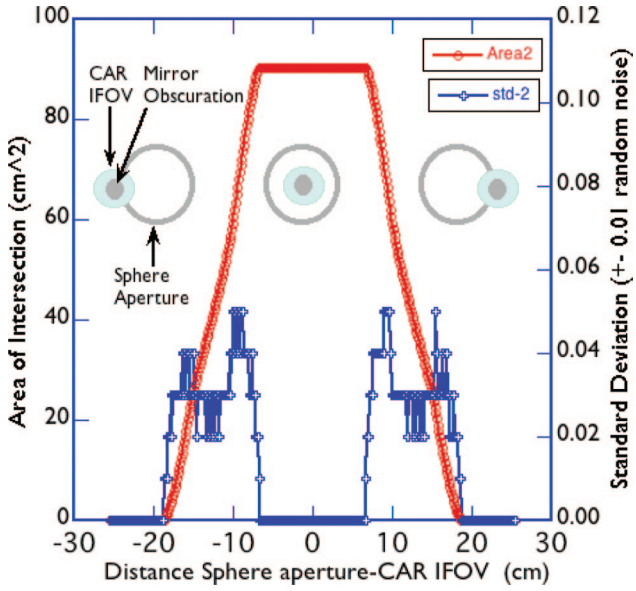

Fig. 13. (Color online) Radiance simulation from a convolution of CAR IFOV (shaded circle with grayish central circle denoting a hollow portion—to denote the CAR telescope's secondary mirror) and sphere aperture (open circle). The area of the sphere aperture that is inside the IFOV (area of overlap) is plotted as a function of the distances between the centers of both circles, thereby defining more accurately the signal strength observed in Fig. 10. Random variations in the distances between the centers of the circles introduce a higher standard deviation (solid curve with + symbol) over the area of partial overlap of the two circles, and has peaks similar to those observed in Fig. 9 from real measurements. (N.B.: size of apertures not drawn to scale.)

Table 5. Variation of Standard Deviation Peaks Relative to their Average Radiance as Function of Distance (%)

	Distance (cm)[a]								
Channel	25.4	45.7	63.5	83.8	106.7	157.5	205.7	332.7	490.2
3	1.2 (0.4)	2.3 (0.9)	3.9 (1.5)	6.0 (1.9)	6.7 (2.6)	12.5 (3.8)	12.3 (4.7)	13.7 (6.8)	14.9
4	1.6 (0.4)	2.6 (0.9)	4.7 (1.6)	5.9 (2.1)	7.6 (2.7)	14.9 (3.9)	13.4 (4.7)	15.6 (7.1)	13.1
5	1.2 (0.3)	2.3 (0.9)	4.0 (1.6)	6.1 (1.9)	8.3 (2.4)	8.9 (3.4)	12.1 (4.8)	20.0 (7.1)	10.8
6	1.2 (0.3)	2.1 (0.9)	4.0 (1.4)	5.3 (1.9)	6.0 (2.4)	10.9 (3.3)	11.3 (4.7)	17.2 (6.6)	10.4
7	1.1 (0.4)	2.2 (1.0)	4.4 (1.6)	5.6 (1.9)	7.3 (2.6)	10.5 (3.3)	10.6 (4.7)	14.8 (5.7)	16.9
8	1.2 (0.9)	2.1 (2.7)	4.2 (1.7)	5.4 (2.7)	7.1 (2.6)	13.3 (2.9)	9.8 (5.2)	14.7 (7.2)	12.6
9	1.2 (0.5)	2.5 (1.0)	4.1 (1.6)	6.2 (1.8)	7.8 (2.9)	9.2 (3.7)	16.4 (4.5)	15.6 (7.4)	10.7
10	1.3 (0.4)	2.4 (1.0)	4.4 (1.7)	5.4 (2.0)	7.0 (2.6)	8.6 (3.6)	11.4 (4.6)	13.8 (6.8)	12.3
11	1.2 (0.4)	2.6 (1.0)	4.1 (1.6)	5.6 (2.1)	7.5 (2.8)	15.2 (4.3)	13.9 (6.0)	13.1 (6.2)	10.4
12	1.3 (0.4)	2.2 (0.9)	4.5 (1.5)	6.3 (2.0)	6.4 (2.5)	12.9 (3.8)	14.4 (5.2)	15.0 (7.3)	12.7
13	1.2 (0.3)	2.6 (0.9)	4.7 (1.7)	6.0 (2.0)	6.7 (2.6)	12.5 (3.8)	13.3 (4.1)	13.6 (6.8)	9.5
14	1.2 (0.4)	2.9 (1.0)	4.1 (1.6)	5.6 (1.8)	6.9 (2.7)	13.2 (4.1)	13.1 (4.0)	13.3 (6.6)	15.5

[a]Values in brackets are for the inner peaks while the rest are for the outer peaks.

fourth peak (outer peaks), while the second and third peaks (inner peaks) are caused by the edge of the telescope's secondary mirror.

Having established the cause of the four standard deviation peaks, each of the peaks was normalized to the corresponding mean radiance, and then averaged separately for the outer and inner peaks as a function of distance from the sphere. Table 5 shows the results of these calculations expressed in percent—the values enclosed in brackets represent a variation due to the secondary mirror (which is an average of the inner peaks), while those outside the brackets represent variations due to the ISS edge (which is an average of the outer peaks). The values for the inner peaks can easily be fitted with a straight line ($y = mx$), where $m = 0.025 \pm 0.005$ for any spectral channel, and x is the separation distance between the instrument aperture and the sphere exit aperture. A similar relationship applies for the outer peaks ($m = 0.065 \pm 0.005$), but only for small separation distances ($x < 150$ cm). The maximum variation from the Slick sphere is seen in channel 5 at $x = 332$ cm (20%), and in channel 2 at $x = 330$ cm from the Uncle sphere (70%). We note that a radiance variation with distance shows a weak spectral dependence.

4. Summary and Conclusions

In this study the problems associated with edge effects of the ISS aperture and the telescope's secondary mirror have been quantified. The random change in the angular speed of the CAR scan mirror and obscuration by the telescope's secondary mirror are the main causes of the radiance variation seen when the ISS aperture enters or leaves the IFOV of the CAR. The secondary mirror of the CAR telescope, which is simulated with a "doughnut" shape, a hole in the center of the CAR IFOV, seems to introduce large variations, especially for distant sources. This appears to be a problem in two mirror systems associated with Cassegrain telescopes. This effect due to the secondary mirror may be described by a linear equation of the form ($y = mx$), where $m = 0.025 \pm 0.005$, and x is the distance between the instrument aperture and the sphere exit aperture. A similar relationship describes the radiance variation due to the sphere edges ($m = 0.065 \pm 0.005$), but only over short distances from the sphere ($x < 150$ cm). Although these effects appear to have little if any impact on calibration accuracy, it is conceivable that the obstruction by the secondary mirror can cause significant errors when scanning a distance source such as the Sun or moon, especially around the edges. It is difficult to detect these edge effects in measurements from an extended diffuse source like the Earth.

The characterization of radiance uniformity across the exit apertures of the three ISS widely used at NASA to calibrate numerous satellite-, aircraft-, and ground-based instruments has been accomplished. The radiance variation across the exit aperture for both the Hardy and Slick spheres is <3% in the visible and near-infrared channels, and <5% in the UV channels for the Hardy sphere and <12% for the Slick sphere. The nonuniformity of the output of the Slick sphere could be due to the fact that the lamps within the sphere are not baffled and the reflectance of the interior of the sphere is nonisotropic due to the use of flat Spectralon panels within the sphere, which may lead to a changing bidirectional reflectance. The spatial radiance gradient for the Uncle sphere in the few channels that are not saturated at the four-lamp level is quite small (<0.4%) and <2% at the two-lamp level. The Hardy sphere, which is used in the calibration of instruments in the visible and near-infrared (0.40–2.40 μm) and the Uncle sphere used primarily in the UV (0.23–0.40 μm) have low spectral radiance gradients across the aperture of less than 2%, as recommended [6], but this seems to depend on the separation distance between the instrument and the ISS.

The responsivity of the CAR instrument across the 190° scan range is <1% in the visible and near-infrared, channels 3–8, but <6% in the UV, channels 1 and 2, at a constant light level and distance from the Slick sphere. The peak radiance seems to depend

on instrument-sphere distance with the Slick sphere showing a change in the UV of 13–20% compared with only 2–5% for the Uncle sphere. In the visible and near-infrared, the change in radiance with distance is generally 5–9%. The cause of radiance change with distance, particularly with the characteristic of having the opposite effect in the UV versus the visible and near-infrared is not clear and needs further investigation.

This research was supported by funding provided by the EOS Project Science Office.

References

1. "Observations from the Nimbus I meteorological satellite," NASA Spec. Publ. 89 (Goddard Space Flight Center, Greenbelt, MD, 1965), 90 pp.
2. W. A. Hovis and J. S. Knoll, "Characteristics of an internally illuminated calibration sphere," Appl. Opt. **22,** 4004–4007 (1983).
3. W. E. Sumpner, "The diffusion of light," Proc. Phys. Soc. London **12,** 10 (1892).
4. J. W. T. Walsh, *Photometry* (Constable, 1958), p. 258.
5. A. C. Hardy and O. W. Pineo, "The errors due to the finite size of holes and sample in integrating spheres," J. Opt. Soc. Am. **21,** 502 (1931).
6. J. H. Walker, C. L. Cromer, and J. T. McLean, "A technique for improving the calibration of large-area sphere sources," Proc. SPIE **1498,** 224–230 (1991).
7. K. Thome, B. Markham, J. Barker, P. Slater, and S. Biggar, "Radiometric calibration of Landsat," Photogramm. Eng. Remote Sens. **63,** 853–858 (1997).
8. http://daac.gsfc.nasa.gov/guides/GSFC/guide/CZCS_Sensor.gd.shtml.
9. C. R. N. Rao, "Pre-launch calibration of channels 1 and 2 of the advanced very high resolution radiometers, NOAA technical report," NESDIS 36 (1987).
10. W. L. Barnes, T. S. Pagano, and V. V. Salomonson, "Prelaunch characteristics of the moderate resolution imaging spectroradiometer (MODIS) on EOS-AM1," IEEE Trans. Geosci. Remote Sens. **36,** 1088–1100 (1998).
11. C. J. Bruegge, V. G. Duval, N. L. Chrien, R. P. Korechoff, B. J. Gaitley, and E. B. Hochberg, "MISR prelaunch instrument calibration and characterization results," IEEE Trans. Geosci. Remote Sens. **36,** 1186–1198 (1998).
12. M. D. King, W. P. Menzel, P. S. Grant, J. S. Myers, G. T. Arnold, S. E. Platnick, L. E. Gumley, S.-C. Tsay, C. C. Moeller, M. Fitzgerald, K. S. Brown, and F. G. Osterwisch," Airborne scanning spectrometer for remote sensing of cloud, aerosol, water vapor, and surface properties," J. Atmos. Ocean. Technol. **13,** 777–794 (1996).
13. B. N. Holben, T. F. Eck, I. Slutsker, D. Tanré, J. P. Buis, A. Setzer, E. Vermote, J. A. Reagan, Y. J. Kaufman, T. Nakajima, F. Lavenu, I. Jankowiak, and A. Smirnov, "AERONET - a federated instrument network and data archive for aerosol characterization," Remote Sens. Environ. **66,** 1–16 (1998).
14. H. Yoon and C. Gibson, "Understanding your calibration sources is the key to making accurate spectroradiometric measurements," OE Mag. **48,** (2001).
15. S. Janz, E. Hilsenrath, J. Butler, D. F. Heath, and R. P. Cebula, "Uncertainties in radiance calibrations of backscatter ultraviolet (BUV) instruments," Metrologia **32,** 637–641, (1995/96).
16. M. D. King, M. G. Strange, P. Leone, and L. R. Blaine, "Multiwavelength scanning radiometer for airborne measurements of scattered radiation within clouds," J. Atmos. Ocean. Technol. **3,** 513–522 (1986).
17. C. K. Gatebe, M. D. King, S. Platnick, G. T. Arnold, E. F. Vermote, and B. Schmid, "Airborne spectral measurements of surface-atmosphere anisotropy for several surfaces and ecosystems over southern Africa," J. Geophys. Res. **108,** doi: 10.1029/2002JD002397 (2003).
18. Cloud Absorption Radiometer: http://car.gsfc.nasa.gov/subpages/index.php?section=Instrument&content=Schematics.
19. F. E. Nicodemus, "Radiance," Am. J. Phys. **31,** 368–377 (1963).
20. S. Brown, NIST, Gaithersburg, MD (personal communication, 2007).
21. E. W. Weisstein, "Circle-Circle Intersection, Equation 14," A Wolfram Web Resource. http://Mathworld.wolfram.com/Circle-CircleIntersection.html.